Comparison of multi-frequency positions of extragalactic sources

Niu Liu[1], Sébastien Lambert[2], Cheng-Yu Ding[1], Zi Zhu[1], and Jia-Cheng Liu[1]

[1] School of Astronomy and Space Science, Key Laboratory of Modern Astronomy and Astrophysics (Ministry of Education), Nanjing University, Nanjing, P. R. China

[2] SYRTE, Observatoire de Paris, Université PSL, CNRS, Sorbonne Université, LNE, Paris, France

Abstract. Previous comparisons of the *Gaia* and radio positions measured by the very long baseline interferometry (VLBI) at *X*-band probes the structure of the milli-arcsecond (mas) scale of Active Galactic Nucleus. But the available VLBI positions at high frequencies are less tapped. We aim to study the multi-frequency position of extragalactic sources, complementary to previous studies We compared the absolute positions measured at four different bands, that is, optical position from the *Gaia* Data Release 2,and three radio position at *X*-, *K*-, and *Ka*-band from the ICRF3 catalog for 488 common sources. We aligned the *K*-band, *Ka*-band, and *Gaia*-CRF onto the *X*-band frame, and then calculated the radio-to-optical offsets. We compared the radio-to-optical offset measured at different bands and correlated them with the magnitude, source structure index, and morphological indices. The absolute difference of radio-to-optical offsets at different radio bands is less than 0.2 mas for 91% of the sample. The large radio-to-optical offset appears to favor faint quasars, while we did not detect obvious correlation on other parameters. We found 57 sources with four-band positions aligned, among which more than half sources have a radio-to-optical offset parallel to their jet when the jet direction is available. However, this position-alignment relation is vulnerable to the global systematics. The source structure does not affect much the radio source position at *X*-band. The selection criteria of optically bright radio-loud sources for frame-link at *X*-band might also work for the *K*- and *Ka*-band. Our result justify the reliability of the ICRF3 *X*-band frame.

1. Introduction

The frequency-dependent position of extragalactic objects (mostly distant quasars) is of interest in both astrometric and astrophysical fields, especially the position offset between the optical centroid and radio core. Such studies can be used to maintain and improve the celestial reference frames materialized by positions of extragalactic objects. For example, the optical observations of the ICRF2 sources in the Rio survey monitors the frame-link status between the *Hipparcos* celestial reference frame and the International Celestial Reference Frame (ICRF) (Assafin et al. 2013). The study of radio-to-optical offset also provides a probing of the structure properties of Active Galactic Nucleus (AGN), such as the accretion disc and relativistic jet (e.g., Plavin et al. 2019).

Accurate positions at sub-milli-arcsecond (mas) are needed for studying the frequency-position relation, which was achieved exclusively by the very long baseline interferometry (VLBI) in the past. The arrival of *Gaia* Data release 2 (*Gaia* DR2; Gaia Collaboration et al. 2016, 2018a) data provides optical positions of quasars with a precision close to their VLBI positions. The comparison between *Gaia* and VLBI positions measured at 8 GHz shows excellent agreements on the level of 1 mas except about 6-9 per cent of outliers, that is, significant *Gaia*/VLBI offsets (Mignard et al. 2016; Gaia Collaboration et al. 2018b; Petrov & Kovalev 2017a,b; Kovalev et al. 2017; Makarov et al. 2017; Frouard et al. 2018; Petrov et al. 2019; Plavin et al. 2019; Kovalev et al. 2020). Recently, Petrov et al. (2019) report that for 62% of sources with a significant *Gaia*/VLBI offset and determinable jet direction, the VLBI-to-*Gaia* offset vector is parallel to the jet. Plavin et al. (2019); Kovalev et al. (2020) further extend this study and find a correlation between the *Gaia*/VLBI offset parallel to jet direction with the dominance of host galaxy, accretion disc, and jet in the optical domain.

These studies, however, are only limited to the VLBI positions at *X*-band. Note that VLBI positions at higher frequencies, such as *K*- and *Ka*-band, are also feasible, showing competing precisions to that of *X*-band (e.g., Jacobs et al. 2019; de Witt et al. 2019). The *K*- and *Ka*-band positions suffer less from the radio source structure and ionosphere and solar plasma effects than at *X*-band (e.g., Jacobs et al. 2002). Including *K*- and *Ka*-band positions in the *Gaia*/VLBI offset studies would help understand the origin of the radio-to-optical offsets. On the other side, the link between *K*- and *Ka*-band VLBI frames and the *Gaia* celestial reference frame (*Gaia*-CRF) also requires detailed studies on the position offsets between *K*- and *Ka*-band and *Gaia*.

We aim to compare the multi-frequency positions of extragalactic sources, in order to complement findings led by Petrov et al. (2019). We computed the *Gaia*/VLBI offsets at *X*-, *K*-, and *Ka*-band and studied their dependency on the astrophysical parameters, such as the magnitude, redshift, source structure at radio and optical domain, in order to provide new insights to understanding of the origin of radio-to-optical, as well as improving the link between *Gaia*-CRF and VLBI frames other than *X*-band.

2. Data and methods

We used the radio positions of quasars measured by VLBI at *X*-, *K*-, and *Ka*-band from the ICRF3 catalog publicly available at the Paris Observatory IERS ICRS Center[1]. For positions of their optical counterparts, we took the *Gaia*-CRF2 sample (gaiadr2.aux_iers_gdr2_cross_id table) from the *Gaia*-

---

[1] http://hpiers.obspm.fr/icrs-pc/newwww/icrf/index.php

DR2 archive[2]. The cross-match amongst these four catalogs gave a list of 488 common sources.

The median formal uncertainties on the right ascension, declination, and along the semi-major axis of error ellipse are $43\,\mu$as, $53\,\mu$as, and $55\,\mu$as, respectively, for the X-band positions. The corresponding values are $66\,\mu$as, $126\,\mu$as, and $128\,\mu$as for their K-band positions; $67\,\mu$as, $98\,\mu$as, and $104\,\mu$as at Ka-band; and $189\,\mu$as, $167\,\mu$as, and $218\,\mu$as for $Gaia$ positions. Therefore, the X-band position precision is generally twice better than the K- and Ka-band, and nearly four times better than the $Gaia$ DR2 positions for the sample used here.

Even the ICRF3 and the $Gaia$-CRF2 are both the realizations of the International Celestial Reference System (ICRS; Arias et al. 1995; Feissel & Mignard 1998), Liu et al. (2020) have revealed some zonal (declination-dependent) errors as large as 0.2 mas in the Ka-band frame, which might bias our analyses here. In order to model and, subsequently, remove these systematical differences, we used the vector spherical harmonics (VSH; Mignard & Klioner 2012) of degree 2, whose equation could be found in Liu et al. (2020, their Eq. (1)). We followed similar procedures described therein to determine 16 transformation parameters between celestial reference frames at different wavelengths, except that we did not perform any outlier elimination. (The influence of outliers on our results are discussed in Sect. 4.3.) The X-band celestial frame was chosen as the reference frame since it is most accurate celestial reference frame so far. By doing so, we permit to analyze multi-wavelength positions in a consist celestial frame and avoid possible bias arising from the alignment and deformation of the celestial reference frames.

We then measured three radio-to-optical offsets, that is, the angular separation between X-, K-, and Ka-band and $Gaia$ positions. We also computed the normalized separation, that is, the X-statistics given in the Mignard et al. (2016), to account for the formal uncertainty and correlation between right ascension and declination of individual sources. These two quantities serve as indicators of significant radio-to-optical offset as done in recent works (e.g., Petrov et al. 2019; Gaia Collaboration et al. 2018b).

In order to study the correlation between radio-to-optical distances and astrophysical properties of the quasars, we used the G magnitude given in the $Gaia$ DR2 catalogs. Besides, we collected the structure index (SI; Fey & Charlot 1997) at X-band from the Bordeaux VLBI Imaging database (BVID) [3] to investigate the effect of the source structure on the radio-to-optical distances. We found 322 matches with the structure index information available. If more than one structure index are given for single sources (observations made more than one epoch), we used the median value. In addition, we retrieved the jet directions of Active Galactic Nucleus from the MOJAVE (Monitoring Of Jets in Active galactic nuclei with VLBA Experiments) survey (Lister et al. 2019, their Table 4).

The fifth release of the Large Quasar Astrometric Catalogue (LQAC-5; Souchay et al. 2019) contains astrometric information for nearly six hundred thousand quasars, where the redshift z and morphological indices (MI) were also included in our analyses. The redshift measurement are given for 443 sources. The morphological index was derived from the B, R, and IR DSS (Digital Sky Survey) images. Three indices are given for each plates, which are SHARP, SROUND, and GROUND index probing skewness, roundness, and normalness of the quasar point spread function, respectively. As suggested by the authos of the LQAC-5 catalogs, these indices can be used to infer the existence

of host galaxy, which might shift the optical position measured by $Gaia$. We found 199 sources associated with the morphological index at the filter B, 396 at the filter R, and 340 at the filter I.

In order to study the relative positions of emission centers at different frequencies, we calculated the position angle (PA) of offsets of K-band, Ka-band, and $Gaia$ positions relative to the X-band position. As illustrated in Fig. 1, the PA is counted as clockwise from the increasing direction of the declination axis.
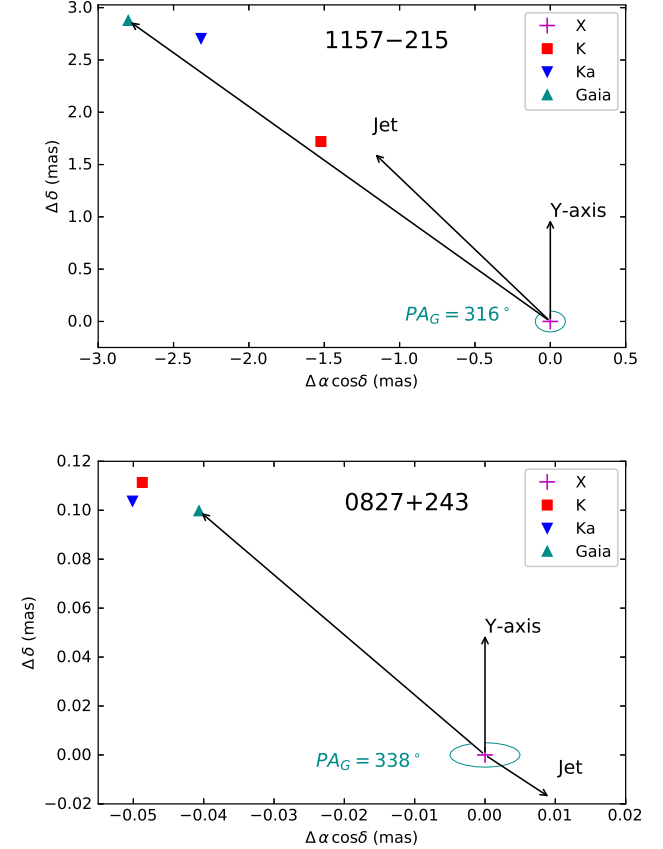

Fig. 1. Illustration diagram of calculation of position angle (*PA*) of offset vectors of K-band, Ka-band, and $Gaia$ (optical) positions with respect to the X-band position for sources (top) 1157–215 and (bottom) 0827+243. The position angle is counted clockwise from the declination axis (Y-axis in the diagram). Also shown is the jet direction for these two sources taken from MOJAVE database (Lister et al. 2019) for comparison whilst the magnitude (length) is arbitrary and thus meaningless.

3. Results

3.1. Removal of large-scale differences

Table 1-2 report the VSH parameters of the first and second degree, respectively. The transformation parameters between K-band and X-band position are less than $30\,\mu$as except D_2 and E_{21}^I. Similar results could be found in between Ka-band and X-band; however, significant terms, D_3, E_{20}, and M_{20} exceeding 0.3 mas are also reported, which would cause a declination bias on the same level. Most of transformation parameters between $Gaia$ and X-band ranges from $30-50\,\mu$as.

Table 1. Rotation and glide and their formal uncertainties of ICRF3 *K*-band, *Ka*-band, and *Gaia*-CRF2 catalogs with respect to the ICRF3 *X*-band catalog.

	No. Sources	R_1 μas	R_2 μas	R_3 μas	D_1 μas	D_2 μas	D_3 μas
$K - X$	793	-15 ± 30	-17 ± 29	$+8 \pm 15$	-17 ± 25	$+51 \pm 26$	$+26 \pm 28$
$Ka - X$	638	-27 ± 11	-2 ± 11	$+17 \pm 7$	$+7 \pm 10$	$+35 \pm 10$	-354 ± 11
$Gaia - X$	2820	$+32 \pm 33$	-47 ± 31	-44 ± 30	-28 ± 32	$+49 \pm 31$	-14 ± 32

Table 2. Quadrupolar terms and their formal uncertainties of ICRF3 *K*-band, *Ka*-band, and *Gaia*-CRF2 catalogs with respect to the ICRF3 *X*-band catalog.

	E^R_{22} μas	E^I_{22} μas	E^R_{21} μas	E^I_{21} μas	E_{20} μas	M^R_{22} μas	M^I_{22} μas	M^R_{21} μas	M^I_{21} μas	M_{20} μas
$K - X$	-2 ± 10	-3 ± 10	-34 ± 29	-71 ± 30	$+7 \pm 33$	$+2 \pm 15$	-11 ± 15	$+15 \pm 30$	-32 ± 30	-26 ± 20
$Ka - X$	-3 ± 5	5 ± 5	-33 ± 12	28 ± 13	86 ± 13	-1 ± 6	$+10 \pm 6$	-7 ± 11	-2 ± 12	224 ± 10
$Gaia - X$	$+37 \pm 19$	-3 ± 19	$+9 \pm 37$	-50 ± 40	$+41 \pm 36$	$+2 \pm 20$	$+1 \pm 20$	$+26 \pm 38$	$+72 \pm 39$	-12 ± 33

Figure 2-4 present the position offset scatter of *K*-band, *Ka*-band, and *Gaia* positions relative to the *X*-band position, as well as distributions of their right ascension and declination components for 488 common sources. The agreement between *K*-band and *X*-band positions is around 0.1 mas on the right ascension; The declination scatter is slightly larger, making the scatter cloud elongating along the declination axis. This phenomenon is more pronounced between *Ka*-band and *X*-band. The distribution of offset between *Gaia* and *X*-band positions, with a nearly circle-like shape, is flatter than the *K*- and *Ka*-band, showing similar agreements of 0.3–0.5 mas on the right ascension and declination. No bias larger than 0.1 mas in the right ascension and declination could be observed for all three position offsets. As a result, we freed studies of multi-wavelength positions carried out in the next sections from large-scale differences.
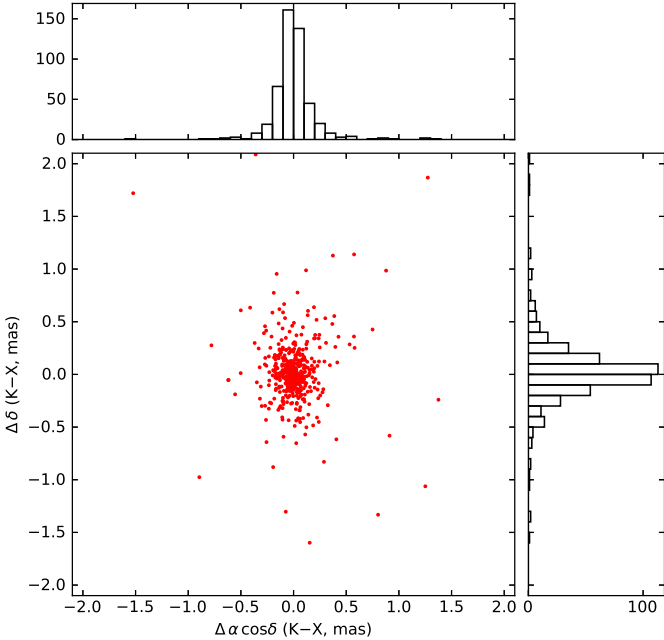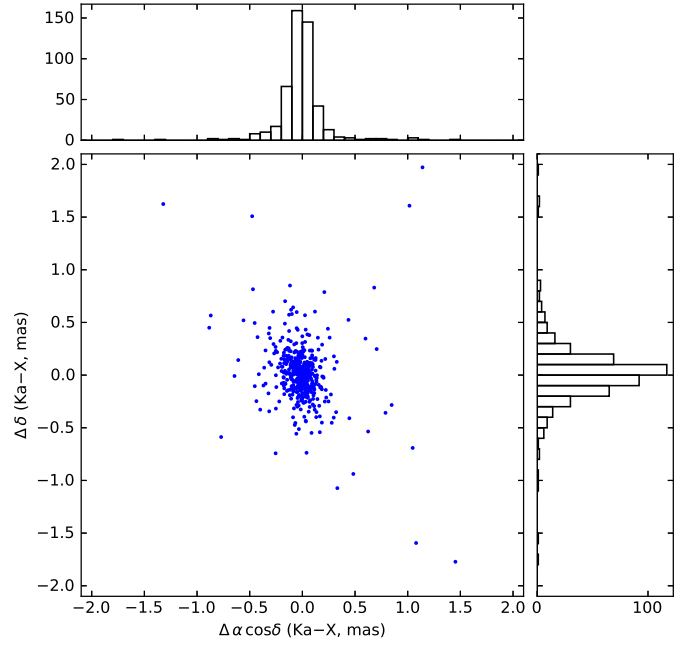

Fig. 2. Position offset scatter and distribution of their component in the right ascension and declination for 488 sources between *X*- and *K*-band positions after removing the global differences, in the sense of "K−X".

Fig. 3. Position offset scatter and distribution of their component in the right ascension and declination for 488 sources between *X*- and *Ka*-band positions after removing the global differences, in the sense of "Ka−X".

3.2. Distribution of radio-to-optical offsets

Figure 5 depicts the distributions of radio-to-optical offsets, yielding a similar shape with an identical median value of 0.41 mas. Only six sources have a radio-to-optical offset larger than 5 mas at either radio bands. We found a second peak at around 0.6 mas at all three bands, which is sharpest at the *X*-band.

The distributions of normalized separations shown in Fig 6 are slightly different: it is sharper for the *Ka*-band while flatter for the *X*-band. There are 16 sources at *X*-band, 6 at *K*-band, and 8 at *Ka*-band with $X > 10$, which are beyond the axis. Medians of normalized separations are 1.89, 1.69, and 1.77 for *X*-, *K*-, and *Ka*-band, respectively, all greater than the median value of 1.18 predicted from a Rayleigh distribution of unit standard
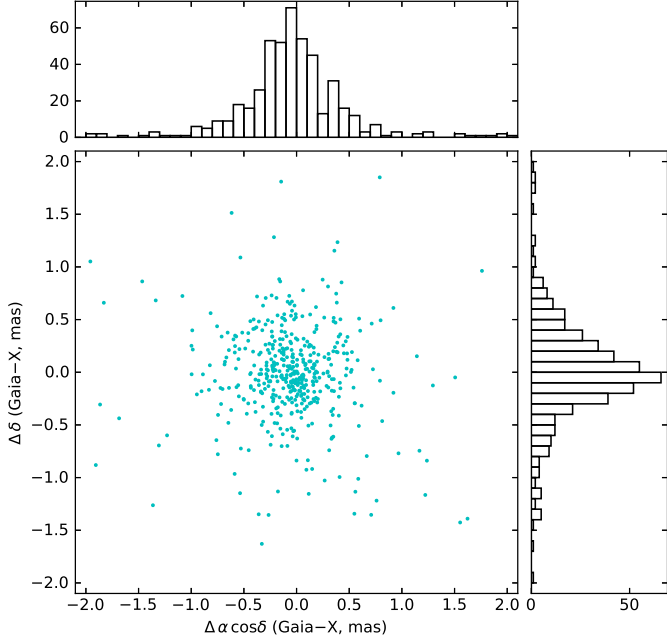
Fig. 4. Position offset scatter and distribution of their component in the right ascension and declination for 488 sources between *X*-band and *Gaia* positions after removing the global differences, in the sense of "*Gaia−X*".

Fig. 5. Distribution of angular separation ρ between the *Gaia* position and VLBI positions at *X*-, *K*-, and *Ka*-band for 488 sources.

deviation. We fitted the normalized separation distributions to the Rayleigh curve with an unknown standard deviation σ. The fitting returns the estimation of σ to be 3.99 for *X*-band, 3.15 for *K*-band, and 3.21 for *Ka*-band. If we made a cut-off of 5 on the normalized separation, σ is estimated to be 1.59 for *X*-band, 1.41 for *K*-band, and 1.46 for *Ka*-band. The distribution of *X* would be closer to the Rayleigh shape if restricting sources to those with $X < 3$, leaving out 138 sources to be outliers for *X*-band, 93 for *K*-band, and 92 for *K*-band.

We further compared three radio-to-optical offsets of individual quasar, as presented in Fig 7-8. Except for few cases, the radio-to-optical offsets determined from *X*-, *K*-, and *Ka*-band generally agrees with each other. Further examinations report 443 sources (91%) with an absolute difference less than 0.5 mas among three radio-to-optical offsets. We observed similar results for normalized separations, regardless the normalized separation at *X*-band is slightly statistically larger than other two bands.

For individual sources, radio-to-optical offsets might be significantly inconsistently. We listed four groups of interest as listed below and discussed them in Sect. 4.1.

A 45 sources with radio-to-radio offsets < 0.5 mas, radio-to-optical offsets > 1 mas.
B 2 sources with *X-Gaia* offset > 1 mas, *K-Gaia* and *Ka-Gaia* offset < 0.5 mas. They are 0723–008 and 2134+004.
C 2 sources with *Ka-Gaia* offset > 1 mas, *X-Gaia* and *K-Gaia* offset < 0.5 mas. They are 1315–058 and 1437+374.
D 2 sources with *K-Gaia* offset > 1 mas, *X-Gaia* and *Ka-Gaia* offset < 0.5 mas. They are 0430–332 and 1611-710.

3.3. Correlation between radio-to-optical offsets and astrophysical parameters

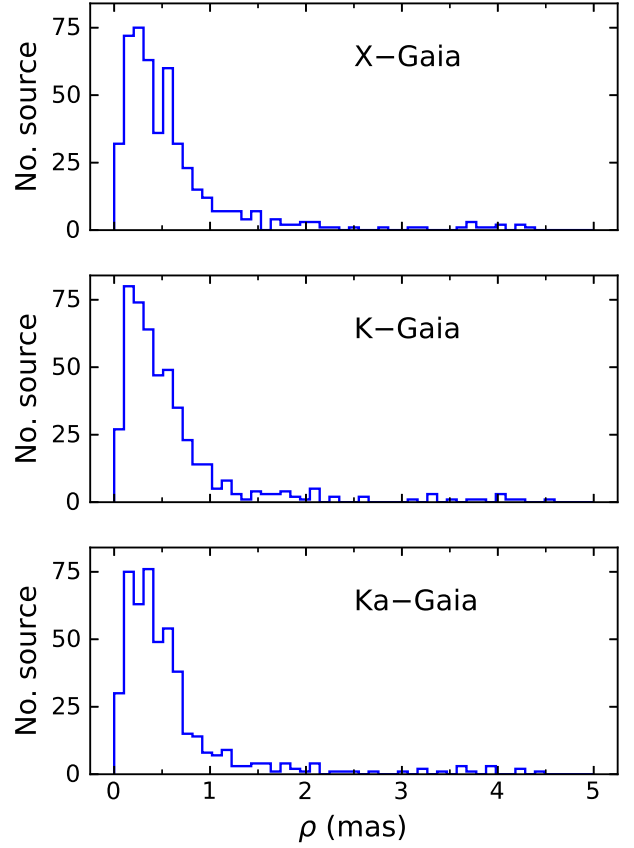Then we studied the correlation between radio-to-optical offsets with astrophysical properties. The radio structure index of 322 sources is color-coded in the Figs. 7-8, where we could not detect a obvious correlation. For most sources, the structure index falls in the range of 2 to 3.5.

Figure 9 demonstrates a correlation between the radio-to-optical offsets and *Gaia G* magnitude: the radio-to-optical offsets increase towards the faint end for all three radio bands. This correlation could be still seen if we included all the common sources between each ICRF catalog and *Gaia*-CRF2 subsets, for instance, the 2820 sources between the ICRF3 *X*-band catalog and *Gaia*-CRF2. We also plotted the normalized separation against the *G* magnitude in the Fig. 10 and found a slightly decreasing trend for *X*-band and flat trends for *K*- and *Ka*-band at $17 < G < 20$. We did not detect any dependency of neither radio-to-optical angular separation (Fig. 11) nor normalized separation (not plotted for brevity) on the redshift.

All three morphological indices larger than one were found for 9 sources at the filter *B*, 16 sources at the filter *R*, and 25 sources at the filter *IR*, corresponding to about 5%, 4% and 7% of the subset with these morphological indices available, respectively. Figures 12-14 demonstrates a smooth dependency of the radio-to-optical distance on the three morphological index of *R*-filter. The morphological index of filter *B* and *IR* present similar results to those of filter *R* and thus are not plotted here.
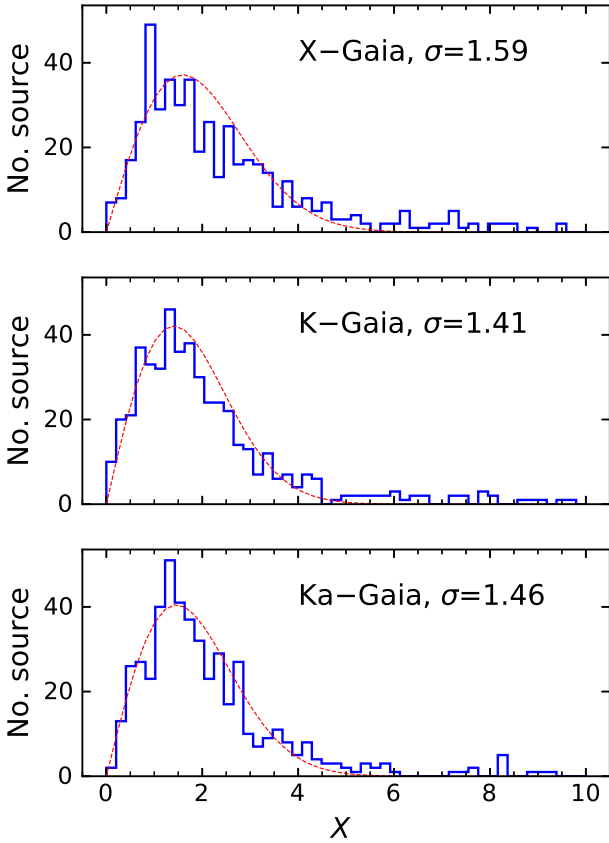
4

Fig. 6. Distribution of normalized separation X between the *Gaia* position and VLBI positions at X-, K-, and Ka-band for 488 sources. The red dashed curves represent standard Rayleigh distributions with a standard deviation of 1.59, 1.41, and 1.46, from top to bottom, respectively.

Fig. 7. Distribution of angular separation ρ between the *Gaia* position and VLBI positions at X-, K-, and Ka-band for 488 sources. The red circles represents 322 sources having a structure index at X-band in the BVID database with the color codes tracing the value of the structure index, while black triangles stand for the other 166 sources.

3.4. Aligned multi-wavelength positions

In this section, we used the direction information of the position offset to investigate the relation of multi-wavelength positions for individual source. The position angles of K-band, Ka-band, and *Gaia* positions with referred to the X-band position are plotted in Fig. 15. Peaks at around $0°$, $180°$, and $360°$ could be observed for K- and Ka-band positions, while *Gaia* position does not show a similar preference.

In order to compare the position angles of K-band, Ka-band, and *Gaia* positions with respective to the X-band position, we calculated the absolute differences between these position angles and wrapped them into the range of $0 - 180°$. Figure 16 depicts the distribution of position angle differences, where one could observe a clear peak around $0°$ above the mean value (red dashed line) while no peak appears at $180°$. If we set a limit on the position angle difference, below which the multi-wavelength positions could be considered as aligned, the number of sources for different cases is summarized in the Table 3. Note that only for sources with all (at least two) normalized separations $X > 1$ with respective to the X-band position, the derived position angle is reliable. Taking this conditions into consideration reduces the subset of sources with aligned positions to nearly their half-size.
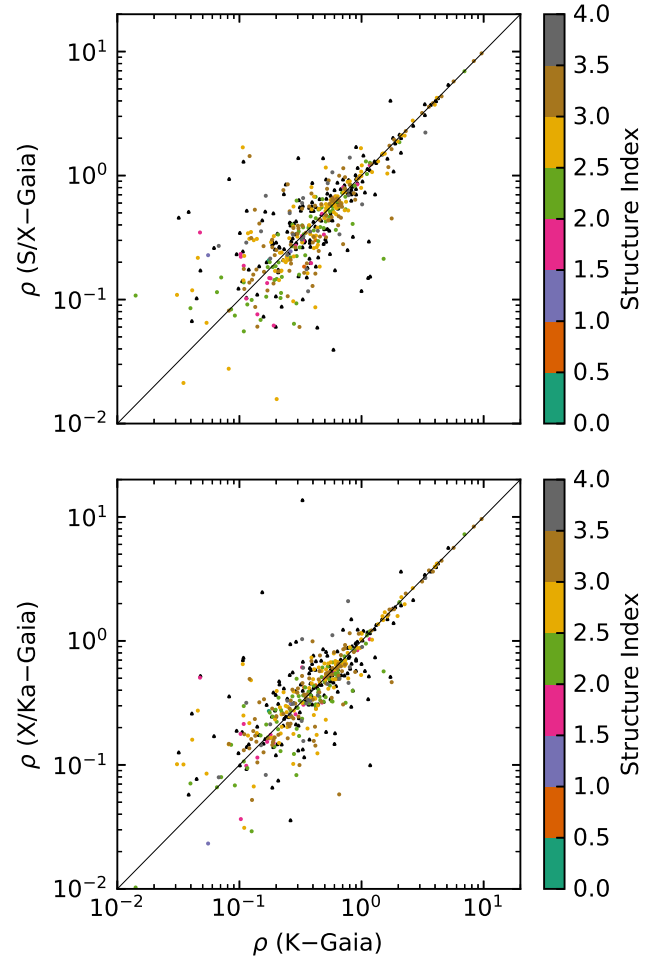
We adopted a limit of $30°$ on the PA difference and the condition of $X > 1$ for further analysis. As a result, we obtained a sample of 54 sources having positions at four frequencies aligned, among which we found the jet information for 23 sources from (Lister et al. 2019). Figure 17 depicts the distribution of the absolute difference between the jet direction and *Gaia*–X offset vector. Again, we considered a PA difference limit of $30°$, therefore, 7 sources have the radio-to-optical offset in the downstream direction while 6 sources with PA difference yields a radio-to-optical offset in the upstream of the jet. Table 4 tabulates the position offsets of K-band, Ka-band, and *Gaia* positions with respective to the X-band position for 54 sources whose four-band positions are aligned.

4. Discussion

4.1. Cause of radio-to-optical distance

Petrov & Kovalev (2017a) summarize several causes for non-coincidence of the emission centers measured by the VLBI and *Gaia*. They includes:

(1) large uncertainties in the *Gaia* or/and VLBI positions;

Table 3. Number of sources with multi-wavelength positions aligned.

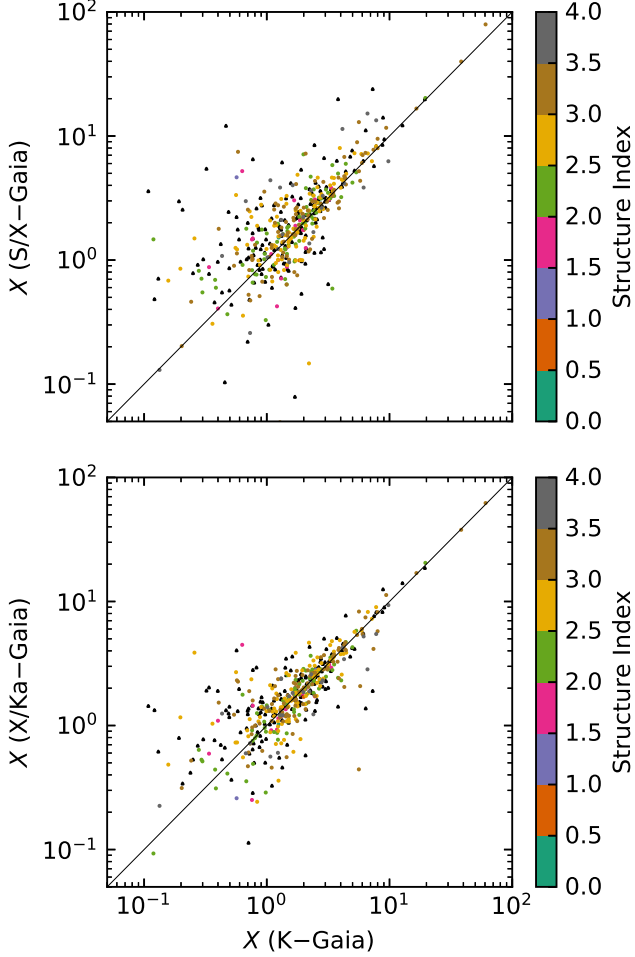|	X, K, Ka	$X, K, Gaia$	$X, Ka, Gaia$	$X, K, Ka, Gaia$
$\Delta PA < 45°$	277	174	170	99
$\Delta PA < 30°$	216	126	124	63
$\Delta PA < 15°$	127	87	76	30
$\Delta PA < 45°, X < 1$	171	96	110	78
$\Delta PA < 30°, X < 1$	135	74	85	54
$\Delta PA < 15°, X < 1$	87	52	56	28

Fig. 8. Distribution of normalized separation X between the *Gaia* position and VLBI positions at *X*-, *K*-, and *Ka*-band for 488 sources. The red circles represents 322 sources having a structure index at *X*-band in the BVID database with the color codes tracing the value of the structure index, while black triangles stand for the other 166 sources.

(2) optical structure (jet) at mas-scale;
(3) optical position shift due to luminous host galaxy or asymmetry structure;
(4) radio source structure and core-shift effect;
(5) gravitational lensing and dual AGNs.
We checked these items based on our results except the second one that has been studied deeply in Kovalev et al. (2017); Petrov & Kovalev (2017b,a); Petrov et al. (2019); Plavin et al. (2019); Kovalev et al. (2020).

The *Gaia* astrometric precision gets worse as one moves to the faint ends, and this holds true for quasar positions (Mignard
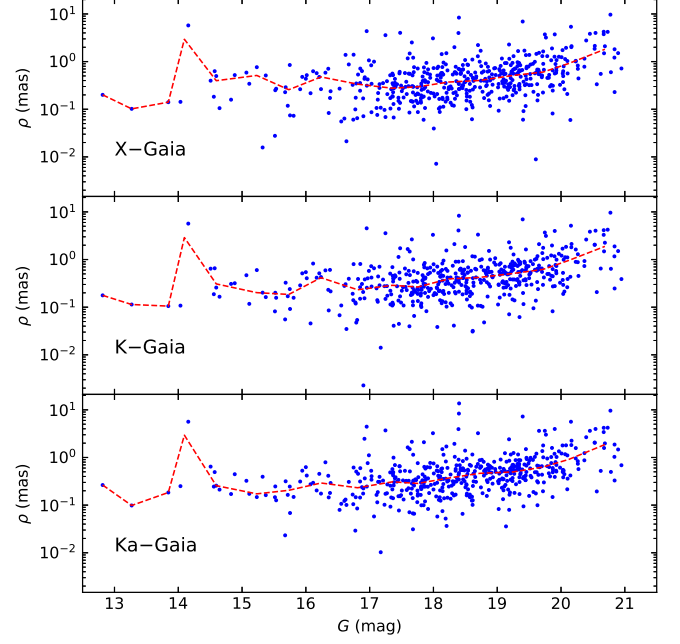

Fig. 9. Angular separation ρ between the *Gaia* position and VLBI positions at *X*-, *K*-, and *Ka*-band as a function of *Gaia G* magnitude for 488 sources. The red dashed line indicates the median values in subsets binned by a step of 0.5 mag.

et al. 2016; Gaia Collaboration et al. 2018b), while VLBI formal error does not yield such a dependency. We observed that the radio-to-optical offsets increase slightly with the *G*-magnitude in the range of $17 < G < 21$, as presented in Fig. 9. It justifies the criterion of being optically bright for selecting suitable optical-to-radio frame-tie sources in Bourda et al. (2008). However, the angular separations between VLBI and *Gaia* positions are flat or even decrease at *X*-band. These results suggest that the large offset at the fainter end are accounted by the *Gaia* formal error, making them less significant.

The radio source structure seen at low frequencies might shift the radio position at *X*-band while the *K*- and *Ka*-band positions are less affected. If the strong source structure exists in the most radio sources, the radio-to-optical distance would significantly decrease at higher frequencies. We did not observe such a tendency; instead, the *X*-, *K*-, and *Ka*-band positions show offsets at the similar level to the *Gaia* position (See Fig. 8). The structure index for sources with a radio-to-optical distance larger than 1 mas mainly exceeds 2.5, suggesting that large radio-to-optical distance is usually associated with a large structure index. It justifies again the selection criterion that frame-tie sources should have a small value of structure index in Bourda et al. (2008).

Table 4. Sources with positions at four bands aligned within 30 °.

IERS name	ρ_K mas	PA_K °	X_K	ρ_{Ka} mas	PA_{Ka} °	X_{Ka}	ρ_G mas	PA_G °	X_G mas	PA_{jet} °	SI	SHARP	SROUND	GROUND
0859-140	0.3	3.1	198	0.2	2.4	207	0.3	3.0	195	178	4.1	0.9	0.4	0.2
1034-293	0.1	0.6	151	0.1	1.3	132	0.5	3.7	140	148	2.4	1.1	0.3	0.3
1157-215	2.3	10.0	318	3.6	8.4	319	4.0	23.9	316	324	-	-	-	-
1222+216	0.2	2.1	11	0.1	1.0	29	0.5	6.3	359	13	-	1.3	0.7	0.9
1742-078	0.4	1.6	186	0.3	1.2	187	1.1	2.6	189	169	3.2	-	-	-
2029+121	0.1	1.6	199	0.2	1.8	173	0.7	1.4	201	183	-	-	-	-
2134+004	1.1	17.2	123	1.3	15.4	123	1.4	19.8	123	96	-	0.0	0.5	0.4
0430+052	0.7	12.9	58	0.7	12.0	60	0.5	11.4	76	258	4.2	0.3	2.6	1.8
0723-008	1.6	15.5	149	1.9	19.3	146	1.4	7.5	148	343	3.3	1.5	1.0	0.6
0743-006	0.3	3.4	220	1.0	14.3	233	1.0	12.9	230	42	3.2	0.6	1.6	0.1
0827+243	0.1	1.3	336	0.1	1.3	334	0.1	1.5	338	152	2.5	0.1	0.5	0.1
0850+581	0.8	6.4	321	0.5	3.7	325	0.8	7.2	337	153	3.2	0.3	0.2	0.2
1038+064	0.2	2.0	348	0.2	2.1	350	0.4	3.8	344	137	3.7	-	-	-
0112-017	0.6	7.6	265	0.6	6.9	283	0.7	4.4	278	146	4.2	0.2	0.1	0.3
0122-003	0.5	2.5	329	0.9	4.2	352	0.6	3.4	358	276	-	1.0	1.1	0.8
0430+052	0.7	12.9	58	0.7	12.0	60	0.5	11.4	76	258	4.2	0.3	2.6	1.8
0528+134	0.1	2.5	279	0.1	1.6	280	0.9	1.3	269	32	2.5	0.6	0.3	2.7
0552+398	0.1	1.7	324	0.2	2.8	323	0.2	1.9	327	358	2.7	0.1	0.3	0.2
0723-008	1.6	15.5	149	1.9	19.3	146	1.4	7.5	148	343	3.3	1.5	1.0	0.6
0743-006	0.3	3.4	220	1.0	14.3	233	1.0	12.9	230	42	3.2	0.6	1.6	0.1
0827+243	0.1	1.3	336	0.1	1.3	334	0.1	1.5	338	152	2.5	0.1	0.5	0.1
0850+581	0.8	6.4	321	0.5	3.7	325	0.8	7.2	337	153	3.2	0.3	0.2	0.2
0859-140	0.3	3.1	198	0.2	2.4	207	0.3	3.0	195	178	4.1	0.9	0.4	0.2
0917+449	0.3	3.2	173	0.3	3.6	160	0.3	3.1	148	197	2.7	1.0	1.0	0.2
0953+254	0.3	4.2	23	0.3	4.5	32	0.8	4.3	49	264	3.2	0.4	0.1	0.5
1034-293	0.1	0.6	151	0.1	1.3	132	0.5	3.7	140	148	2.4	1.1	0.3	0.3
1038+064	0.2	2.0	348	0.2	2.1	350	0.4	3.8	344	137	3.7	-	-	-
1157-215	2.3	10.0	318	3.6	8.4	319	4.0	23.9	316	324	-	-	-	-
1222+216	0.2	2.1	11	0.1	1.0	29	0.5	6.3	359	13	-	1.3	0.7	0.9
1611+343	0.3	5.1	202	0.2	2.4	198	0.3	4.1	180	113	3.1	0.4	0.5	0.1
1742-078	0.4	1.6	186	0.3	1.2	187	1.1	2.6	189	169	3.2	-	-	-
2029+121	0.1	1.6	199	0.2	1.8	173	0.7	1.4	201	183	-	-	-	-
2113+293	0.1	1.7	253	0.1	1.2	230	0.8	3.1	247	198	-	0.4	0.9	0.3
2134+004	1.1	17.2	123	1.3	15.4	123	1.4	19.8	123	96	-	0.0	0.5	0.4
2234+282	0.4	6.3	225	0.3	5.4	221	0.5	3.0	224	151	-	0.2	0.6	0.6
2251+158	0.4	7.2	76	0.3	4.4	69	0.5	8.5	70	280	-	0.1	0.7	0.5

Notes. Sources are divided into three groups: (Top) *Gaia* positions in the downstream of jet with respect to the *X*-band positions; (Middle) *Gaia* positions in the upstream of jet; (Bottom) others. The first column gives the source name of IERS designation . The columns 2-4, 5-7, 8-10 present the angular separation ρ, normalized separation X, and position angle of *K*-X, *Ka*-X, and *Gaia*-X offset. The column 11 contains the jet direction collected from the Table 4 in Lister et al. (2019), followed by the source structure index provided by BVID database. The last three columns list the morphological index, namely, SHARP, SROUND, and GROUND, at R filter taken from the LQAC-5 catalog. The "-" symbol means that the corresponding information is not available.

We picked out sources according to their radio-to-radio and radio-to-optical offsets in Sect. 3.2. For sources in the group A, radio cores all locate far from the optical core, indicating that the radio-optical offset is more likely related to the shift of optical position. We compared our list with those in Makarov et al. (2017, their Table 1), and found that 4 sources were labeled as "galaxy" and 2 sources were recognized as double component therein. The former case means that the optical centroid measured by *Gaia* is perturbed by the luminous host galaxy or asymmetry dust structures. As for two sources in the gourp B, the possible explanation is that *Gaia* measures position of the same radio component as the *K*- and *Ka*-band do, while the *X*-band measures another one. Similar explanations also works for the group C and D.

Since there are only few cases with larger morphological indices than 1, the influence of the host galaxy on the *Gaia* position, if exist, is not significant for the bulk of our sample. Since these indices were determined from the optical imaging with a resolution of arc-seconds or worse, we could not use them to probe the mas-scale optical jet. Morphological indices based on high-resolution images might be useful to infer the existence of the mas-scale optical jet found by Petrov & Kovalev (2017b).

4.2. Frequency-position relation

We found 54 sources, 11% of the sample, showing roughly aligned positions at four frequencies. Among these sources, 13 out of 23 sources (> 50%) with available jet direction informa-
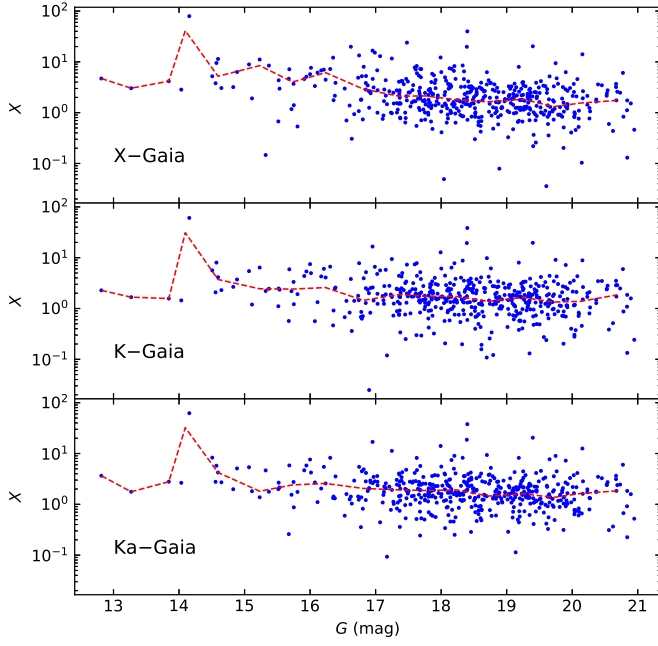
Fig. 10. Normalized separation X between the *Gaia* position and VLBI positions at X-, K-, and Ka-band as a function of *Gaia G* magnitude for 488 sources. The red dashed line indicates the median values in subsets binned by a step of 0.5 mag.
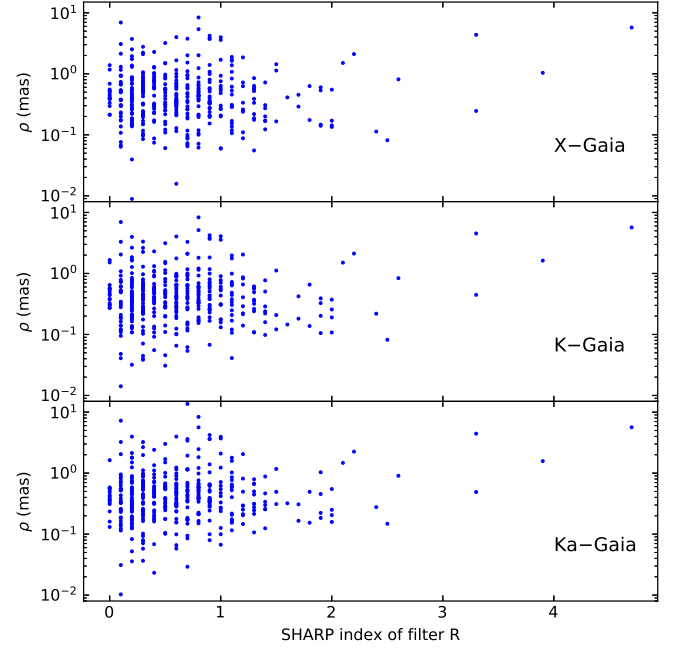

Fig. 12. Angular separation ρ between the *Gaia* position and VLBI positions at X-, K-, and Ka-band as a function of morphological SHARP index at filter R for 396 sources having R-filter morphological indices in the LQAC-5 catalog.
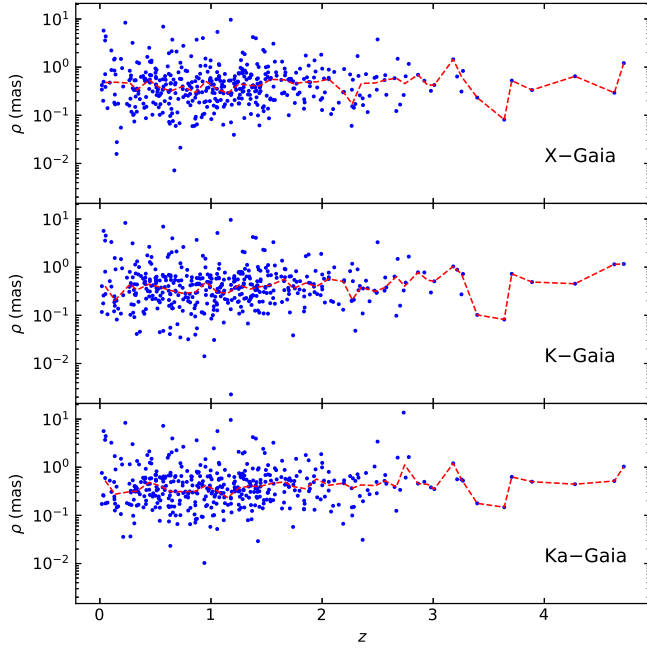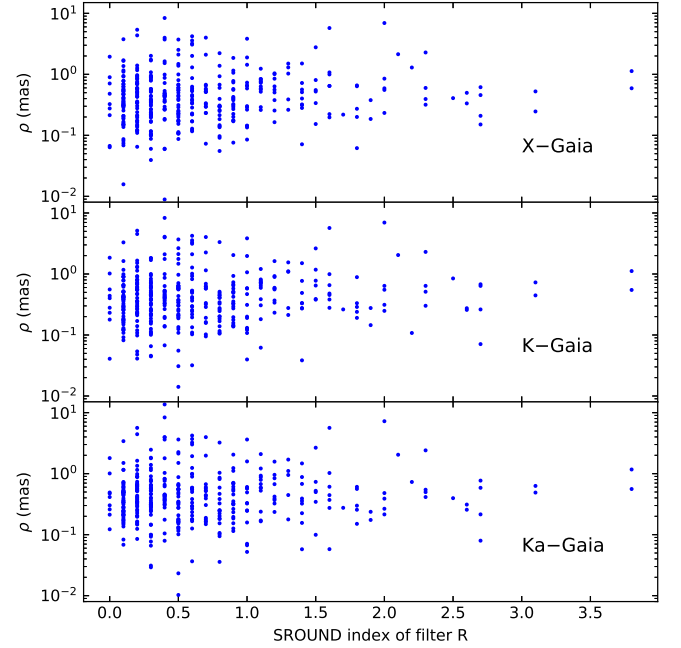

Fig. 11. Angular separation ρ between the *Gaia* position and VLBI positions at X-, K-, and Ka-band as a function of red-shift z for 443 sources having a red-shift measurements in the LQAC-5 catalog. The red dashed line indicates the median values in subsets binned by a step of 0.1.

Fig. 13. Angular separation ρ between the *Gaia* position and VLBI positions at X-, K-, and Ka-band as a function of morphological SROUND index at filter R for 396 sources having R-filter morphological indices in the LQAC-5 catalog.

tion have the radio-to-optical vector parallel to the jet vector. If this result holds true for a large sample, it might serve an astrometric method of determining the jet direction.

The core-shift effect produces a frequency-dependent shift along the jet between the radio core and the jet base. It suggests that the multi-wavelength quasar positions would follow a sequence of *Gaia–Ka–K–X* towards to the jet downstream. However, only few sources follows such a position sequence, for example, 1157–215 as shown in the upper panel of Fig. 1. We assumed that the *Gaia* position to be the jet base and fitted the three radio positions of 1157–215 to the core-shift relation
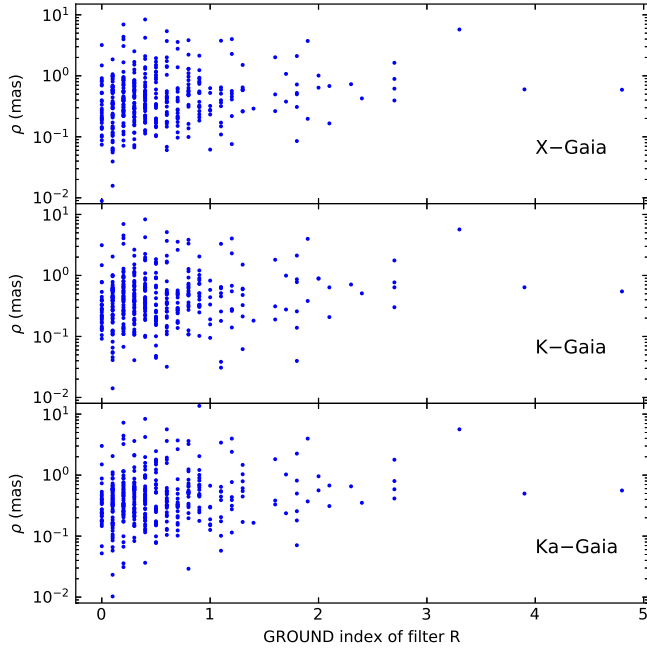
Fig. 14. Angular separation ρ between the *Gaia* position and VLBI positions at *X*-, *K*-, and *Ka*-band as a function of morphological GROUND index at filter R for 340 sources having R-filter morphological indices in the LQAC-5 catalog.
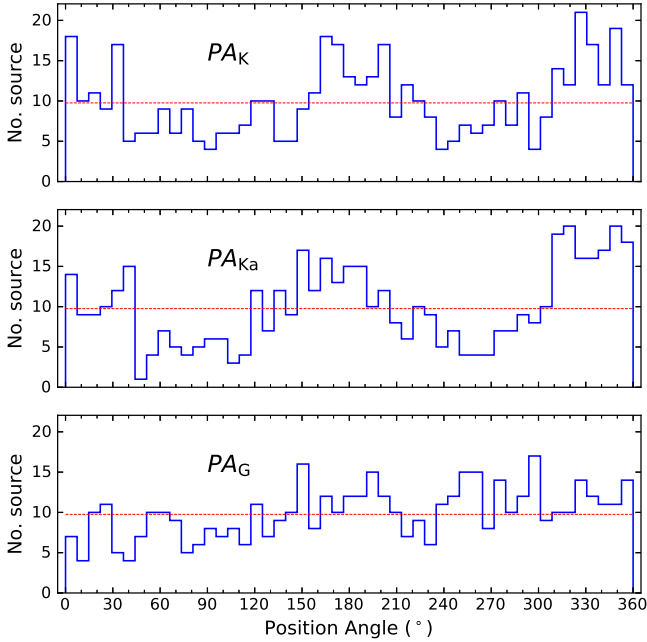

Fig. 16. Distribution of the absolute position angle difference of offset vector of *K*-band, *Ka*-band, and *Gaia* positions with referred to the *X*-band position for 488 common sources. The horizontal red dashed line stands for a uniform distribution.

Fig. 15. Distribution of the position angle of offset vector of *K*-band, *Ka*-band, and *Gaia* positions with referred to the *X*-band position for 488 common sources. The horizontal red dashed line stands for a uniform distribution.
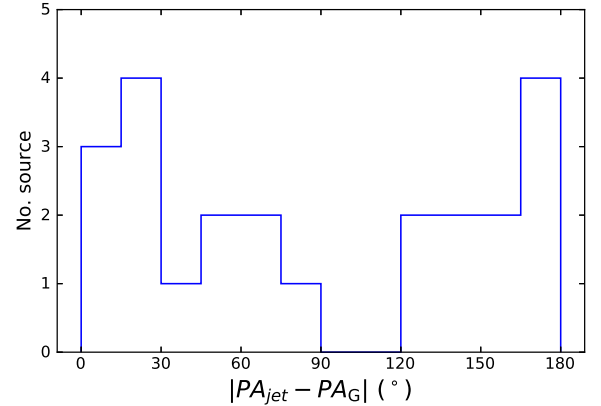
Fig. 17. Distribution of the absolute position angle difference of *K*−*X* position offset vector and jet vector for 23 sources whose four-band positions are almost aligned ($\Delta PA < 30°$).

4.3. Influence from the large-scale difference

Our previous work reports that the global differences amongst ICRF3 and *Gaia*-CRF2 catalogs would bias the radio-to-optical offset studies (Liu et al. 2020). Therefore, we removed the global difference of *K*-band, *Ka*-band, and *Gaia*-CRF2 frames relative to the *X*-band frame via all the common sources between these three catalogs and *X*-band catalogs. If this procedure is omitted, we would observe a declination bias ~ -0.3 mas in the *Ka*-*X* position offset, while *K*-*X* and *Gaia*-*X* offsets are less affected. The peaks around 180° in the position angle of *K*-*X* and *Ka*-*X* offset shown in Fig 16 would be more pronounced. Moreover, we would not have chance to see four positions located in a line for more than 50 sources.

$r(\nu) = r_0 \cdot \nu^{-k}$. The fitting shows the spectral index to be nearly −1, which differs from the result of $k = 1$ as predicted in Porcas (2009); Kovalev et al. (2008). However, our simple derivation of the spectral index k is far from robust and reliable. But it worths revisiting the core-shift effect when the new VLBI solutions or *Gaia* data are published.
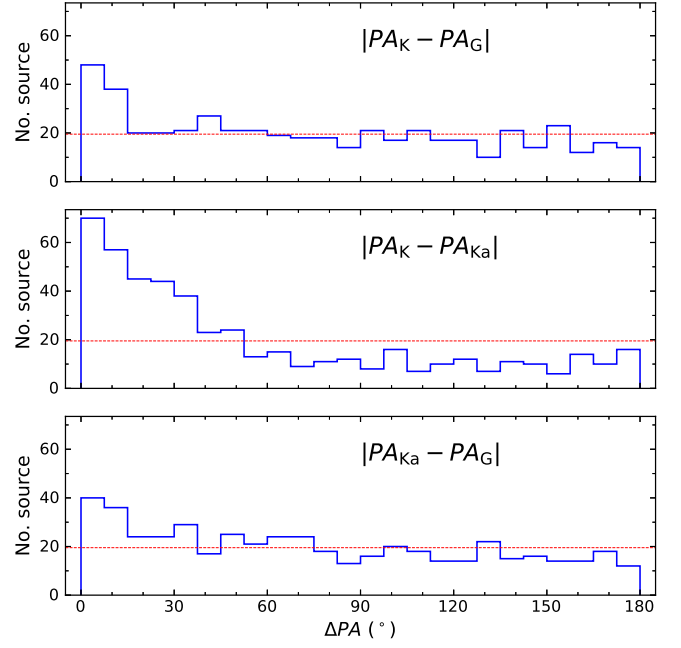
The global differences between celestial frames at different wavelengths could also be modeled on a "clean" sample selected from the all common sources, as done in Liu et al. (2020). If doing so, a glide term D_3 of Ka-band frame would be reduced to about $-200\,\mu$as. Consequently, the sharp peak around $0°$ depicted in Fig. 16 becomes flatter, especially for the position angle difference between Ka–X and $Gaia$–X offsets. On the one hand, it indicates that such a alignment amongst four-frequency positions is sensitive to the global systematics. On the other hand, this result also justifies the reliability of the ICRF3 X-band frame, otherwise, the alignment might be biased by the frame deformation or other systematics.

5. Conclusion

We compared the positions of 488 extragalactic sources at radio X-, K-, Ka-band and in optical domain in order to study the frequency-position relation, especially the radio-to-optical offset. The radio positions were taken from the ICRF3 catalog and the optical position was retrieved from the *Gaia* DR2. We found:

(1) Radio-to-optical distance is at the same level estimated (difference less than 0.2 mas) at X-, K-, and Ka-band for 90% of the sample. There are 45 sources show good agreements among three radio positions but large radio-to-optical offsets. For few cases, the *Gaia* position matches radio potions of only two bands.
(2) Large radio-to-optical distance (> 1 mas) is usually associated with a large source structure index (> 3).
(3) The radio-to-optical distance increases at the fainter end but would be accounted for by the increasing *Gaia* formal errors.
(4) About 11% (54 sources) of the sample show four-band position aligned, which is in parallel to the jet for 13 out of 23 sources with the jet direction data.

The traditional criteria of selecting optically bright sources for the ICRF at X-band and *Gaia*-CRF link, e.g., Bourda et al. (2008); Makarov et al. (2019), might also suit the frame-tie between K- and Ka-band frames and *Gaia*-CRF.

The alignment of multi-frequency positions suggests a possible astrometric method of determining the jet direction of AGNs. However, this alignment is vulnerable to the global systematic in the celestial frame, especially the Ka-band. We anticipate to revisit such a relation when a more accurate Ka-band solution is released and more jet direction determinations are available. Our results, in the other hand, justify that the ICRF3 X-band frame is accurate and reliable.

References

Arias, E. F., Charlot, P., Feissel, M., & Lestrade, J. F. 1995, A&A, 303, 604
Assafin, M., Vieira-Martins, R., Andrei, A. H., Camargo, J. I. B., & da Silva Neto, D. N. 2013, MNRAS, 430, 2797
Bourda, G., Charlot, P., & Le Campion, J. F. 2008, A&A, 490, 403
de Witt, A., Gordon, D., Jacobs, C. S., et al. 2019, in Proceedings of the 24th European VLBI Group for Geodesy and Astrometry Working Meeting, ed. R. Haas, S. Garcia-Espada, & J. A. López Fernández, P306
Feissel, M. & Mignard, F. 1998, A&A, 331, L33
Fey, A. L. & Charlot, P. 1997, ApJS, 111, 95
Frouard, J., Johnson, M. C., Fey, A., Makarov, V. V., & Dorland, B. N. 2018, AJ, 155, 229
Gaia Collaboration, Brown, A. G. A., Vallenari, A., et al. 2018a, A&A, 616, A1
Gaia Collaboration, Mignard, F., Klioner, S. A., et al. 2018b, A&A, 616, A14
Gaia Collaboration, Prusti, T., de Bruijne, J. H. J., et al. 2016, A&A, 595, A1
Jacobs, C. S., Garcia-Mrio, C., Horiuchi, S., et al. 2019, in Proceedings of the 24th European VLBI for Geodesy and Astrometry (EVGA, ed. R. Haas, S. Garcia-Espada, & J. A. López Fernández, P302
Jacobs, C. S., Jones, D. L., Lanyi, G. E., et al. 2002, in International VLBI Service for Geodesy and Astrometry: General Meeting Proceedings, ed. N. R. Vandenberg & K. D. Baver, 350
Kovalev, Y. Y., Lobanov, A. P., Pushkarev, A. B., & Zensus, J. A. 2008, A&A, 483, 759
Kovalev, Y. Y., Petrov, L., & Plavin, A. V. 2017, A&A, 598, L1
Kovalev, Y. Y., Zobnina, D. I., Plavin, A. V., & Blinov, D. 2020, MNRAS, 493, L54
Lister, M. L., Homan, D. C., Hovatta, T., et al. 2019, ApJ, 874, 43
Liu, N., Lambert, S. B., Zhu, Z., & Liu, J. C. 2020, A&A, 634, A28
Makarov, V. V., Berghea, C. T., Frouard, J., Fey, A., & Schmitt, H. R. 2019, ApJ, 873, 132
Makarov, V. V., Frouard, J., Berghea, C. T., et al. 2017, ApJ, 835, L30
Mignard, F. & Klioner, S. 2012, A&A, 547, A59
Mignard, F., Klioner, S., Lindegren, L., et al. 2016, A&A, 595, A5
Petrov, L. & Kovalev, Y. Y. 2017a, MNRAS, 471, 3775
Petrov, L. & Kovalev, Y. Y. 2017b, MNRAS, 467, L71
Petrov, L., Kovalev, Y. Y., & Plavin, A. V. 2019, MNRAS, 482, 3023
Plavin, A. V., Kovalev, Y. Y., & Petrov, L. Y. 2019, ApJ, 871, 143
Porcas, R. W. 2009, A&A, 505, L1
Souchay, J., Gattano, C., Andrei, A. H., et al. 2019, A&A, 624, A145